ASSESSMENT AND IMPROVEMENT OF PREDICTIVE MODELS FOR ESTIMATING SHIP DRAG PENALTIES FROM CALCAREOUS BIOFOULING ROUGHNESS

Isnain 'Aliman, Jelle Will, Bagus Nugroho, Jason Monty & Nicholas Hutchins
Department of Mechanical Engineering
University of Melbourne
Parkville, Victoria 3010, Australia
inoviar@student.unimelb.edu.au

ABSTRACT

Calcareous biofouling, such as barnacles, shells, and tubeworms, on the ship's hull can significantly increase hydrodynamic resistance, yet predictive models for estimating the equivalent sandgrain roughness due to hull roughness are rarely validated against realistic biofouling surface geometries. To address this gap, a real biofouling roughness topography, scanned directly from a ship hull, was replicated and tested in a wind tunnel, with surface statistics systematically varied by changing the barnacle density. Comparison with the experimental results shows that a modified Forooghi *et al.* (2017) roughness correlation, refitted in terms of k_{rms} using a broader training dataset, predicts the equivalent sand-grain roughness (k_s) with good agreement. The obtained k_s values were further extrapolated to ship scale to estimate real-world drag penalties, highlighting the potential increase in resistance from calcareous biofouling roughness.

1 INTRODUCTION

Field experiments were conducted on the tanker ship MT. Sinar Morotai, documenting skin friction and hull condition over the past 4 years since its last dry-docking in March 2022. During the first two years of sailing, the cleaned and recoated sections of the hull remained free of hard fouling thanks to the applied self-polishing copolymer coating. This consistent hull condition resulted in a constant measured skin-friction drag penalty, $\Delta\overline{C_f}(\%) = 100 \times (\overline{C_f}_{rough} - \overline{C_f}_{smooth})/\overline{C_f}_{smooth}$, of approximately 30 % over the same period. However, during dry-docking the vessel was supported by sleepers, leaving roughly one hundred $0.2 \times 1\,\mathrm{m}^2$ rectangular patches on the underside of the hull that were neither cleaned nor recoated. These so-called docking-block regions are therefore prone to accelerated fouling by algae, tube worms, shells, and barnacles. Photogrammetry reconstructions of these regions, acquired using the AQUAMARS device (Kevin *et al.*, 2025), an image-based diver-operated underwater scanner, were analyzed in this study. The roughness statistics for these docking block observations, characterized in terms of skewness (S_k) and effective slope (ES) of the measured roughness statistics, are shown by the orange circles, clustered in the shaded orange region of the roughness parameter space map shown in Figure 2. The biofouled surfaces generally lie within the lower effective-slope range, $ES < 0.4$, while spanning a broad range of skewness, $-0.5 < S_k < 5.5$.

The ultimate aim of this study is to evaluate and improve

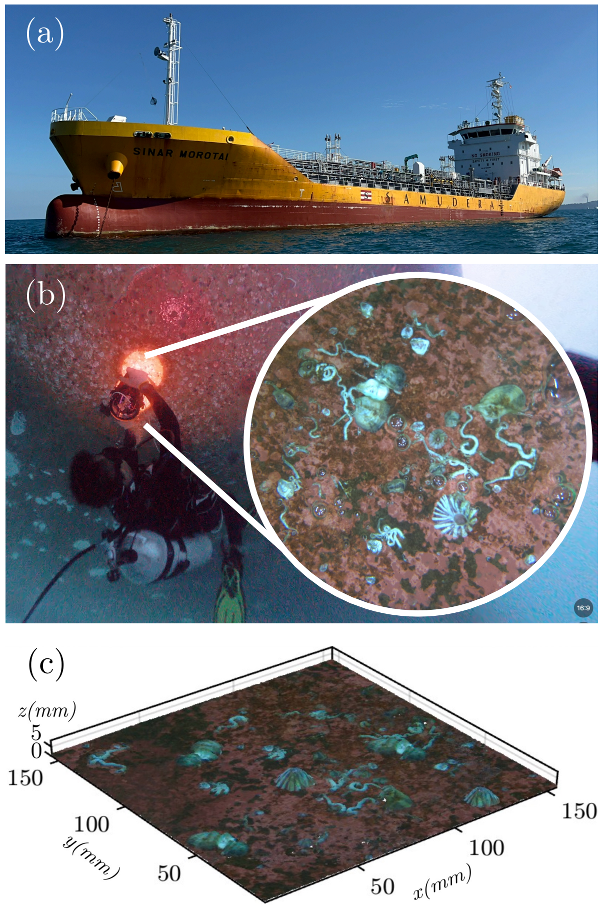

Figure 1. (a) MT. Sinar Morotai, a chemical tanker on which field experiments have been conducted since March 2022, with skin friction and hull condition monitored regularly. (b) Divers operating AQUAMARS to capture roughness samples from the ship's hull. AQUAMARS is an in-house, image-based underwater 3D scanner developed at the University of Melbourne that simultaneously captures the target from multiple angles. The 3D surface is then obtained through photogrammetric reconstruction. (c) Reconstructed surfaces of the selected roughness samples to be tested in the wind tunnel. This sample was captured from the docking-block areas and contains key calcareous biofouling features, including barnacles, shells, and tubeworms.

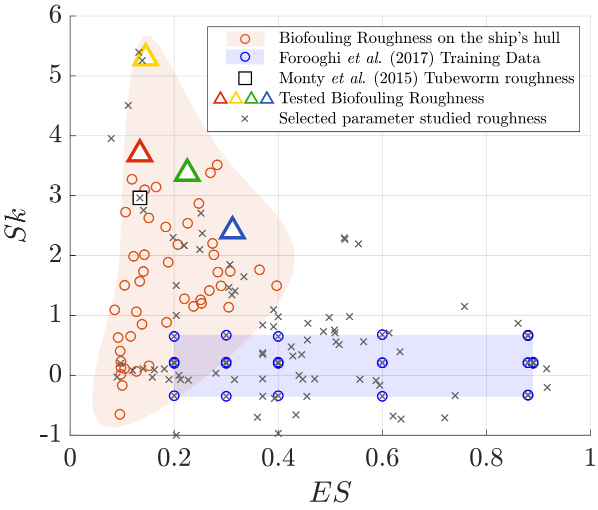

Figure 2. Distribution of roughness statistics in the *ES*–*Sk* parameter space. The orange symbols and region show biofouling roughness scanned using the underwater 3D scanner. The blue symbols and region indicate training data used by Forooghi *et al.* (2017) to develop their predictive correlation. Grey crossed symbols represent various selected roughness studies including Schlichting (1937), Monty *et al.* (2016), Squire *et al.* (2016), Flack *et al.* (2016), Forooghi *et al.* (2017), Barros *et al.* (2018), Flack *et al.* (2019), Flack *et al.* (2020), Jouybari *et al.* (2021), Womack *et al.* (2022), and Medjnoun *et al.* (2023). .

the use of predictive correlations to estimate the equivalent sand-grain roughness (k_s), which provides a common basis for comparing the hydraulic effects of different rough surfaces. In this sense, k_s acts as a common roughness currency, allowing surfaces with very different morphologies to be compared according to 'how rough they are' as experienced by the flow. For ship-hull roughness, estimating k_s is essential because it links measured surface scans to the resulting drag penalty. However, the accuracy of these correlations, especially for biofouled surfaces, which are multiscaled and range from dense to sparse arrangements, remains largely untested. Chung *et al.* (2021) reviewed existing predictive correlations for estimating k_s, such as Macdonald *et al.* (1998), Chan *et al.* (2015), Forooghi *et al.* (2017), and Flack *et al.* (2019). Chung *et al.* (2021) also suggested that a good model should incorporate three key aspects of roughness of: (a) roughness height (k_a, k_{rms}, k_t, or $\bar{k}_t$); (b) frontal solidity λ_f, effective slope ES, or roughness density parameter Λ_s; and (c) plan solidity λ_p, skewness Sk, or solid volume fraction ϕ. Among the available correlations, Forooghi *et al.* (2017) provides a useful starting point, as it is formulated in terms of three roughness parameters: the average peak-to-trough height ($\overline{k_t}$), effective slope (ES), and skewness (S_k). The blue circle symbols associated with the blue shaded region in Figure 2 indicate the training data used to formulate the original correlation of Forooghi *et al.* (2017). However, compared with the orange-shaded biofouling region, the training data provide poor coverage of the parameter space associated with the docking-block roughness statistics.

Determining which predictive correlation can accurately estimate k_s requires validation against realistic biofouling roughness. However, the available k_s data for realistic biofouling remain limited, with the tube worm roughness studied by Monty *et al.* (2016), shown as the rectangular symbol in Figure 2, being one of the few available cases. Obtaining k_s is not straightforward, as it is not simply a geometric height parameter, but an effective scale inferred from the flow response over the rough surface, typically from wind-tunnel experiments or direct numerical simulations. The grey crossed symbols represent the selected roughnesses that have been studied extensively in the fluid mechanics literature. These surfaces have been examined either experimentally in tunnels or numerically using DNS, often up to the fully rough regime. While some of these roughnesses overlap with the biofouling *ES*–*Sk* parameter space, most are synthetic and do not represent realistic biofouling geometries. Accordingly, the aim of this study is to replicate and measure k_s for realistic biofouling surfaces reconstructed from docking-block scans. Expanding the number of tested realistic biofouling surfaces within the ES–S_k parameter space will provide a stronger basis for assessing and improving predictive correlations for k_s, and help address a key challenge in estimating ship drag penalty from hull surface scans, by avoiding the need for costly experimental and numerical procedures to obtain k_s in the future.

2 METHODOLOGY

In this study, the roughness scan shown in Figure 1(c), acquired from the docking blocks of the MT. Sinar Morotai, is selected for reproduction and wind-tunnel testing. Figure 3(c) shows the corresponding surface height map for this scan. The sample features small and large barnacles, tube worms, and shells, as well as substrate roughness. The surface in Figure 1 is the tessellation unit that undergoes filtering, expansion, and cropping to produce a 150x150 mm square area. This surface is plotted as the yellow triangle in Figure 2. To extend the outcomes of this study, the selected scan was populated with additional barnacle features by filling the empty space to form Surface 1 (see Figure 3a) as the initial test geometry, and plotted as a blue triangle in Figure 2. After performing experiments on Surface 1, half of the barnacles were removed to create Surface 2 (Figure 3b) plotted as a green triangle in Figure 2. It is important to note that the removed barnacles will reveal the underlying substrate topography. This enables a systematic investigation of the effect of barnacle population density on roughness, extending the $ES-Sk$ coverage of the results while reducing experimental cost by minimizing test-plate manufacturing. Further removal of barnacles recovered the original scanned sample Surface 3, shown in Figure 3(c). Finally, Surface 4, depicted in Figure 3(d) with a red triangle in Figure 2, has all barnacles removed, leaving only sparse shells and tube worms.

Experiments were conducted in an open-return boundary-layer wind tunnel at the University of Melbourne's Walter Bassett Laboratory. The test surface covers an area of $0.8 \times 4\,\mathrm{m}^2$ and is assembled from four $0.8 \times 1, \mathrm{m}^2$ test plates, and the final setup is shown in Figure 4(a). Each plate is manufactured using a CNC machine from 12 mm thick Acetal plates with an aperiodic tessellated roughness surface generated from the repeating unit shown in Figure 3. To prevent the formation of coherent flows structures caused by large-scale periodicity, as reported by Nugroho *et al.* (2021), the tessellation strategy is designed to produce a random, aperiodic pattern by arranging square tessellation units over a $0.8 \times 1\,\mathrm{m}^2$ area by rotating and flipping them randomly. To avoid the streamwise alignment of prominent biofouling features, such as barnacles, the tessellation units are also shifted in the spanwise direction. The four tessellation units shown in Figure 3 are processed using the same tessellation procedure, producing surfaces that share

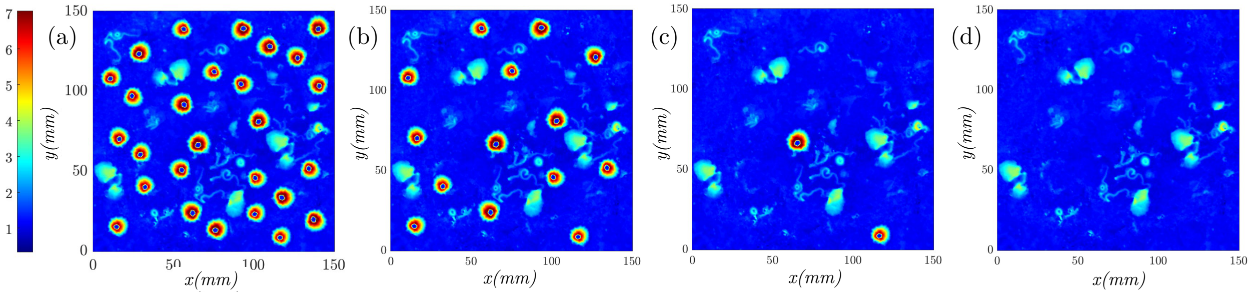

Surface and Symbol	Roughness Statistics					Lab Results (Drag Balance)		Original Forooghi *et al.* (2017) model, Case I		Modified Forooghi *et al.* (2017) model Case II		Modified Forooghi *et al.* (2017) model Case III		Windshade model	
	ES	S_k	k_{rms} (mm)	k_t (mm)	$\overline{k_t}$ (mm)	$k_{\mathrm{s\text{-}lab}}$ (mm)	$\Delta\overline{C_f}$ (%)	$k_{\mathrm{s\text{-}pred}}$ (mm)	$\Delta\overline{C_f}$ (%)	$k_{\mathrm{s\text{-}pred}}$ (mm)	$\Delta\overline{C_f}$ (%)	$k_{\mathrm{s\text{-}pred}}$ (mm)	$\Delta\overline{C_f}$ (%)	$k_{\mathrm{s\text{-}pred}}$ (mm)	$\Delta\overline{C_f}$ (%)
1 = △	0.31	2.40	1.30	7.49	7.33	10.3	171	38.6	263.5	13.8	188.5	10.6	172	18.3	207
2 = △	0.22	3.37	0.98	7.49	7.28	6.90	149	51.1	288.5	9.58	166.9	7.32	152	7.20	151
3 = △	0.14	5.06	0.54	7.49	5.69	2.55	105	57.1	299.0	4.23	126.2	3.39	116	0.72	63
4 = △	0.13	3.69	0.40	4.30	3.74	1.30	81	20.6	214.9	2.65	106.7	1.99	96	0.15	27

Figure 3. Unit tile or repeating unit of the biofouling roughness surfaces prior to tessellation, the reported roughness statistics, estimated $k_{s-\mathrm{pred}}$ from the correlations in Table 1, and the estimated ship drag penalty $\Delta\overline{C_f}$. The subset area, $h \times h$, for calculating $\overline{k}_t$, uses $h = \delta_{99}$ obtained from the CTA measurements. (a) Surface 1, densely populated with barnacles; (b) Surface 2, with approximately half of the barnacles removed; (c) Surface 3, the original scanned surface characterized by high skewness (S_k) and low effective slope (ES); and (d) Surface 4, with all large barnacle features removed, leaving only shells and tubeworms.

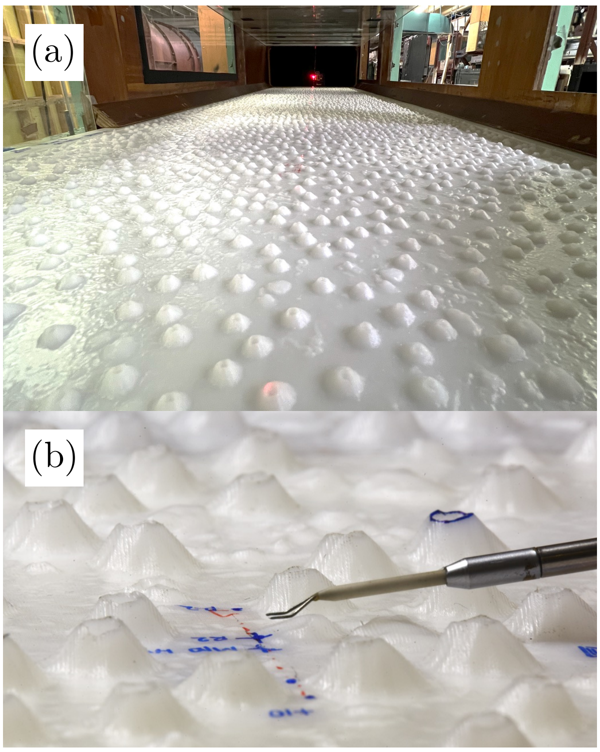

Figure 4. (a) The manufactured biofouling surfaces (Surface 4) installed in the wind tunnel for testing. (b) CTA sensor placed above the biofouling roughness, which is located at 3.82 m from the inlet of the tunnel.

the same underlying tube worm and shell topographies, with variation arising only from the barnacle features. This approach also makes it easier for the CNC machine to remove selected barnacle features, allowing the surface to be modified efficiently.

Measurements were taken at 3.9 m (middle section of the DB plate) downstream of the tripped entry to the working section. Direct skin friction measurements at different streamwise Reynolds numbers $C_f(Re_x)$ were obtained by varying the freestream velocity in the facility using a cantilever-type drag balance from the 2×3 repeating unit under the zero pressure gradient condition. While the surrounding plates are modified by removing barnacles, the drag-balance plates are manufactured individually to ensure high manufacturing accuracy. Details of the balance, its operation, and the pressure-moment correction are provided in Ramani *et al.* (2024). Based on the same study, the experimental uncertainty of this drag balance is $\pm 4\%$ at the highest Re_x. Constant-temperature (hot-wire) anemometry (CTA) was used to obtain boundary-layer profiles of streamwise velocity over these roughness surfaces. A photograph of the CTA sensor above the manufactured biofouling test surface is shown in Figure 4(b). A Melbourne University Constant Temperature Anemometer (MUCTA) with 5μm platinum Wollaston wire sensor ($l/d = 200$) was used (Perry, 1982). Fluctuating voltage signals from the anemometer were sampled for 30 s (boundary layer turnover time $T_s U_\infty/\delta_{99} \gtrsim 8\,400$, statistically converging mean and variance) at 40 logarithmically spaced wall-normal locations on the center of the drag balance plate. Boundary layer profiles were made at a minimum of 9 spanwise locations covering 40 mm in the span, which is approximately twice the calculated in-plane spanwise wavelength of these rough surfaces.

3 WIND TUNNEL RESULTS OF THE TESTED BIOFOULING ROUGHNESS

The wall shear stress, τ_w, for each roughness case was measured directly using the cantilever drag balance, from which the skin-friction coefficient, $C_f = 2\tau_w/(\rho U_\infty^2)$, was calculated as a function of $Re_x = U_\infty x/\nu$ as shown in Figure 5(a). The scatter in C_f from nine repeated measurements for each surface is shown as dots, all of which fall within the shaded coloured region corresponding to the expected $\pm 4\%$ uncertainty of the drag balance (Ramani *et al.*, 2024). The C_f for

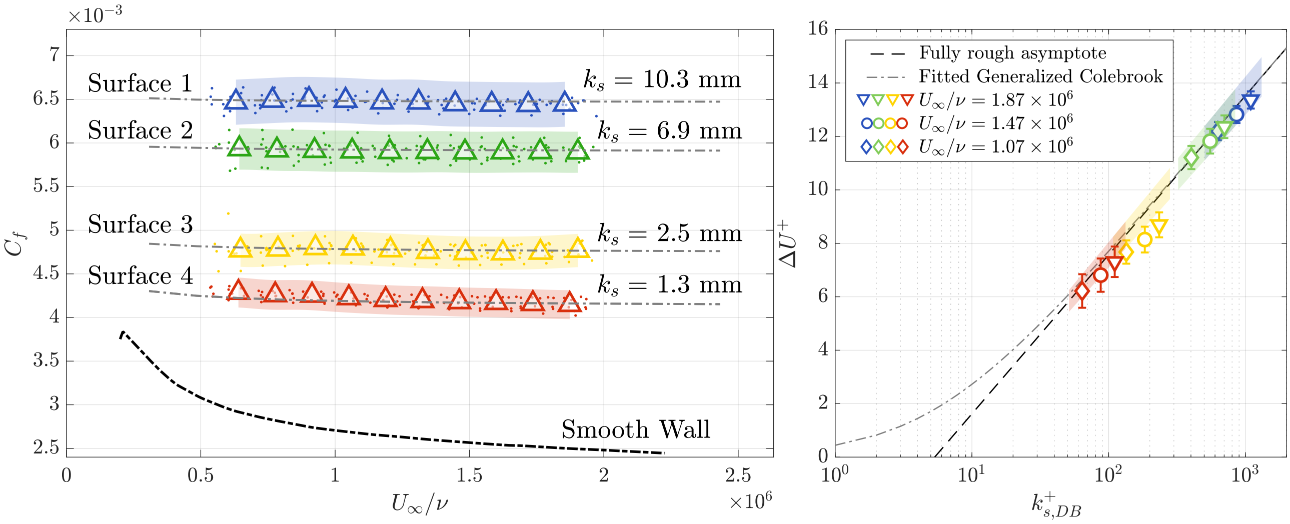

Figure 5. Wind tunnel experiment results of the tested biofouling roughnesses. (a) Drag balance measurements of the skin-friction coefficient, C_f, as a function of unit Reynolds number, U_∞/ν. The color (refers to Figure 3) represents the four tested biofouling surfaces. (b) Comparison of the roughness function obtained from HWA measurements, ΔU^+, and the k_s^+ is obtained from the drag balance. Symbols represent the U_∞/ν of the HWA measurements. The dashed line shows the fully rough asymptote ($\kappa = 0.384, A = 4.17, B = 8.5$), while the grey dot dashed line shows the Fitted Generalized Colebrook to the drag balance data. The collapse of the symbols onto the dashed line indicates good agreement between the drag balance results and the HWA results.

each result is averaged, as shown by the colored triangle symbols, to yield the final result. At the highest Reynolds numbers, all cases exhibit a fully rough regime, evidenced by $C_f(Re_x)$ becoming approximately independent of Re_x. The k_s of each result can be estimated by matching the $C_f(Re_x)$ curve measured from the drag balance to that predicted by a standard Integral Boundary Layer Evolution (IBLE) technique of Monty *et al.* (2016). A composite mean streamwise velocity profile from Chauhan *et al.* (2007) and a wake strength $\Pi = 0.43$, which matches well with the smooth- and rough-wall HWA data, is used to make this IBLE prediction. The roughness function used in the IBLE is the generalized Colebrook function (Cheng *et al.*, 2020), where $U^+ = \frac{1}{p\kappa}, \log\left(1+\beta(k_s^+)^p\right)$, and $\beta = \exp(\kappa(A-B))$, $A = 4.17$, $B = 8.5$m and $p = 1$. In practice, however, this choice is inconsequential here, because k_s is determined by matching the drag-balance data at the highest Re_x, where all tested surfaces are effectively fully rough. A fully rough asymptotic form would therefore give essentially the same estimated k_s. The value of k_s was obtained by repeating the IBLE prediction over a range of assumed k_s and selecting the best match to the measured drag-balance data. This analysis indicates that the tested biofouling surfaces correspond to k_s values ranging from 1.3 to 10.3 mm.

An alternative approach to determining k_s could be to derive the Hama roughness function (ΔU^+) directly from the measured mean velocity profiles. The profiles were nondimensionalized using the friction velocity measured by the drag balance measurements ($u_{\tau,\mathrm{DB}} = U_\infty\sqrt{C_f/2}$) resulting in the normalised mean profile $U^+ = \overline{u}/u_{\tau,\mathrm{DB}}$ vs $z_\varepsilon^+ = (z+\overline{\varepsilon})u_{\tau,\mathrm{DB}}/\nu$. The virtual origin, $\overline{\varepsilon}$, was defined as the mean of the values obtained at each spanwise location, where the individual virtual origin was chosen to produce the best logarithmic fit with slope $1/\kappa$ over the range $0.08\delta_{99}^+ < z^+ < \delta_{99}^+/6$. This subsequently allowed us to extract ΔU^+ from the viscous-scaled profiles by comparing the shift between the rough- and smooth-wall profiles at the outer edge the logarithmic region, $z^+ = \delta_{99}^+/6$. Figure 5(b) shows the value of ΔU^+ extracted in this way against k_s^+ inferred from the drag balance. The black dashed line shows the fully rough asymptote, while the gray dashed-dot line shows the fitted generalized Colebrook function fitted to the drag balance data. The error bars on the plotted symbols show the variation of ΔU^+ to one standard deviation for the 9 spanwise measurements. The shaded color represents the uncertainty of the drag balance measurements and the range of k_s^+ explored in the measurements. From this figure, within the measurement uncertainty, most HWA obtained data points lie reasonably close to the fully rough asymptote and the shaded region from the drag balance. The exception is surface 3, where the HWA measured ΔU^+ are slightly lower than expected. Given the highly skewed surface type and sparse roughness, it is plausible that the limited spanwise HWA survey did not fully capture the average roughness effect. The drag-balance measurement is therefore considered more representative as it reflects the mean of the integrated drag over a 2×3 repeating unit.

4 ASSESMENT OF THE EXISTING PREDICTIVE CORRELATION

The biofouling surfaces tested here provide a basis for evaluating the performance of predictive methods by comparing the k_s estimated from correlations with those inferred from laboratory measurements. A natural starting point for assessing the existing predictive correlations is the model of Forooghi *et al.* (2017), as it is formulated in terms of the three roughness parameters highlighted by Chung *et al.* (2021) and was developed using training data covering a broader range of ES and S_k than the other available correlations. Other available correlations, such as Macdonald *et al.* (1998), Chan *et al.* (2015), and Flack *et al.* (2019) have already been tested against the lab results; however, since they are not tailored based on ES and S_k independently, and the available training data coverage is limited, the results are not discussed in this study.

The Forooghi *et al.* (2017) correlation is written as

$$\frac{k_s}{k_{\mathrm{option}}} = \left(a_2 S_k^2 + a_1 S_k + a_0\right) b \left(1 - e^{-cES}\right), \qquad (1)$$

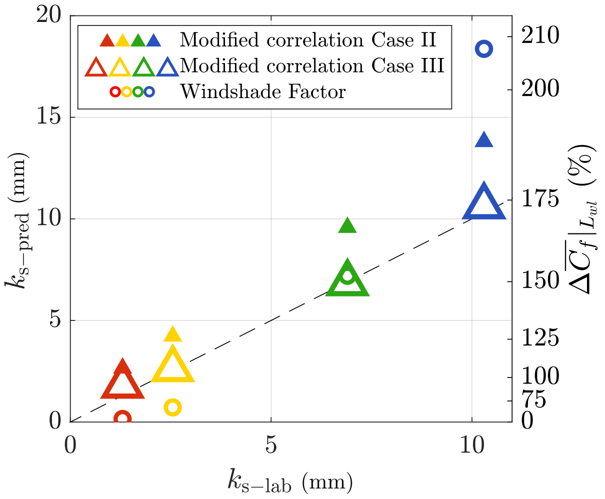

Figure 6. Comparison between the k_s inferred from the laboratory experiments ($k_{s-\mathrm{lab}}$) and that predicted using the correlation ($k_{s-\mathrm{pred}}$) for the tested biofouling surfaces (fitting coefficients for different Cases of modified Forooghi *et al.* (2017) correlation are summarised in Table 1). The black dashed line denotes the 1:1 agreement line. The small filled triangles represent the modified Forooghi *et al.* (2017) correlation Case II, while the big open triangles represent Case III. The small open circle denotes the $k_{s-\mathrm{pred}}$ using the Windshade factor method from Meneveau *et al.* (2024). The right-hand axis shows the corresponding $\Delta\overline{C_f}$ obtained using the IBLE method under the operating conditions of MT. Sinar Morotai.

where, for the original Forooghi *et al.* (2017) correlation, $k_{\mathrm{option}} = \overline{k_t}$, the mean peak-to-trough roughness height. The corresponding constants are listed in Table 1 as Case I. Forooghi *et al.* (2017) mentioned that the normalization with $\overline{k_t}$ provided the best collapse of the original training data; However, the inclusion of $\overline{k_t}$ introduces a degree of arbitrariness that limits the applicability of this correlation in industry, since $\overline{k_t}$ is, by definition, an outlier with poor statistical convergence and is highly dependent on the chosen subset size and sampling approach. Especially for the calcareous biofouling roughness, $\overline{k_t}$ is dominated by the largest feature (barnacles in this case), often resulting in an overprediction of k_s. The estimated k_s from the tested biofouling cases using this original correlation is presented in the Table in Figure 3.

Replacing $\overline{k_t}$ with a more robust, statistically converged roughness height measure can substantially improve the predictive correlation by removing the arbitrariness associated with subset selection. Accordingly, the original predictive model of Forooghi *et al.* (2017) was modified by refitting the same training dataset, replacing the original formulation $k_s/\overline{k_t}(ES,S_k)$ with $k_s/k_{rms}(ES,S_k)$, while retaining the original functional form. The fitted constants for this modification are shown in Table 1 as Case II. Even though the estimation of the tested biofouling surfaces by using this modified predictive correlation requires substantial extrapolation (See shaded blue vs shaded orange area in Figure 2), this model can predict k_s reasonably well for the tested biofouling surfaces compared to the original model in Case I (See the table below Figure 3 for estimated $k_{s-\mathrm{pred}}$ vs $k_{s-\mathrm{lab}}$ comparison). Figure 6 shows the estimated k_s relative to the lab results using the Case II fit plotted as the small filled triangles. These predictions lie close to the black dashed line, indicating good agreement between the laboratory-derived k_s and the predicted values.

Table 1. Fitted constants of the original and modified Forooghi *et al.* (2017) predictive correlation for different roughness-height normalizations and levels of training-data coverage. Case I: The Original Forooghi *et al.* (2017) correlation. Case II: Modified Forooghi *et al.* (2017) fitted k_{rms} with Forooghi *et al.* (2017) original training data. Case III: Modified Forooghi *et al.* (2017) fitted k_{rms} with broader training data plotted in grey-x symbols in Figure 2. Case IV: final recommended fit in which the tested biofouling surfaces were incorporated into the Case III training dataset.

Case	Function	a_2	a_1	a_0	b	c
I	$k_s/\overline{k_t}$	0.670	0.93	1.30	1.07	3.50
II	k_s/k_{rms}	-0.052	0.55	0.68	10.78	2.76
III	k_s/k_{rms}	-0.330	2.81	3.36	2.30	1.86
IV	k_s/k_{rms}	-0.346	2.82	3.37	2.33	1.82

Since refitting the original predictive correlation of Forooghi *et al.* (2017) from $k_s/\overline{k_t}$ to k_s/k_{rms} improved its ability to estimate k_s for the tested biofouling surfaces, the next step is to assess whether its predictive performance can be further improved by expanding the training dataset to include more surfaces that fall within the orange shaded region. The aim is to better anchor the correlation over a broader *ES–Sk* parameter space and thereby improve its applicability to biofouling surfaces. To do this, the correlation in equation 1 is refitted using all data represented by the grey crossed symbols in Figure 2, which correspond to the selected results from the literature. Our tested biofouling surfaces are not included in this fit, so they can be used independently to assess the method's validity. The resulting constants are summarised in Table 1 as Case III. The open, larger triangle symbols in Figure 6 show the k_s values predicted using this updated correlation. These symbols lie even closer to the black dashed line, indicating improved predictive performance for biofouling-type surfaces. Finally, the tested biofouling surfaces were included in the fitting procedure, producing the coefficients reported as Case IV, which are recommended for estimating k_s of biofouling roughness. Relative to Case III, the fitted coefficients change only marginally, and the estimated k_s by Case IV remains almost the same (4% maximum difference in Surface 4), suggesting that the broader correlation remains consistent after the present biofouling surfaces are included.

Unlike other predictive correlations that relate k_s to measured roughness parameters such as ES, S_k, and characteristic roughness length scales, the wind-shade model of Meneveau *et al.* (2024) takes a physics-based approach by explicitly accounting for the sheltering effects of roughness elements. Using this method, the estimated k_s values for the tested biofouling roughnesses are shown as circle symbols in Figure 6. It can be seen that the method provides reasonable agreement only for Surface 2. For Surface 1, corresponding to the highest-density biofouling roughness, the method over predicts k_s. By contrast, for the sparser roughnesses of Surfaces 3 and 4, the predicted k_s is lower than that inferred from the laboratory measurements.

The k_s values obtained from the assessed predictive methods were then extrapolated to ship scale to estimate the associated drag penalty, as shown on the right-hand axis of Figure 6. The previously described IBLE approach was used to integrate the increase in local C_f along a representative length of the ship hull. Here, the operating condition of MT. Sinar Morotai is considered, with a waterline length of $L_{wl} = 92.7$ m. The vessel cruising speed is taken as 5.12 m/s, corresponding to the average speed recorded during the first three field campaigns. The working fluid is seawater, with a kinematic viscosity of $\nu_{\mathrm{sea}} = 8.42 \times 10^{-7}$ m^2/s.

From the estimated drag penalty, it can be seen that differences in predicted k_s have a much larger effect on $\Delta\overline{C_f}$ for the lower-k_s cases than for the higher-k_s cases. This is because during the early stages of biofouling accumulation, when the hull departs from a hydrodynamically smooth condition, the estimated drag penalty increases rapidly with increasing roughness (since ΔU^+ is proportional to $\log k_s$). For example, the modified Forooghi correlation Case III predicts a k_s of approximately 10 mm for the roughest biofouling case, which is close to the laboratory-inferred value and corresponds to a drag penalty of around 172%. By contrast, the wind-shade method predicts a larger k_s of approximately 18 mm, but this increases the estimated drag penalty only to about 205%. For the smoothest laboratory case, Surface 4, which consists only of tube worms and shells, the estimated $\Delta\overline{C_f}$ ranges much more widely, from approximately 10% to 80%, depending on the predicted k_s. Thus, the main implication of Figure 6 is that accurate prediction of k_s is especially important for the lower-roughness cases, where relatively small differences in k_s can lead to large differences in the estimated drag penalty.

5 CONCLUSIONS AND OUTLOOK

The results of this study show that the modified Forooghi *et al.* (2017) correlation, refitted in terms of k_{rms} and trained on a broader dataset, provides a practical and accurate way to estimate k_s for realistic calcareous biofouling roughness. This provides a useful link between measured hull condition and the resulting ship drag penalty. The wind-tunnel experiments of the replicated scans with the barnacle density variation demonstrated that the tested surfaces span a substantial range of k_s values from 1.3 to 10.3 mm, which corresponds to 81-171% drag penalty compared to the hydrodynamic smooth wall. Extrapolation of the predicted k_s values to ship scale further shows that uncertainty in k_s estimation can lead to substantial differences in the predicted drag penalty, particularly for the lower-roughness cases. Overall, the results support the use of the proposed predictive correlation as a practical route for estimating ship drag penalty from realistic hull scans, while future work should validate the resulting drag-penalty predictions against what is measured from the field measurements. The current work on this validation is presented in Will *et al.* (2026).

REFERENCES

Barros, J. M., Flack, K. A. & Schultz, M. P. 2018 Measurements of skin-friction of systematically generated surface roughness. *Int. J. Heat Fluid Flow* **72**, 1–7.

Chan, L., MacDonald, M., Chung, D., Hutchins, N. & Ooi, A. 2015 A systematic investigation of roughness height and wavelength in turbulent pipe flow in the transitionally rough regime. *J. Fluid Mech.* **771**, 743–777.

Chauhan, K. A., Nagib, H. & Monkewitz, P. A. 2007 On the composite logarithmic profile in zero pressure gradient turbulent boundary layers. In *45th AIAA Aerospace Sciences Meeting and Exhibit, Reno, NV*, , vol. 1, pp. 532–549.

Cheng, W., Pullin, D. I. & Samtaney, R. 2020 Large-eddy simulation and modelling of taylor–couette flow. *J. Fluid Mech.* **890**, A17.

Chung, D., Hutchins, N., Schultz, M. P. & Flack, K. A. 2021 Predicting the drag of rough surfaces. *annu. Rev. Fluid Mech.* **53**, 439–471.

Flack, K. A., Schultz, M. P. & Barros, J. M. 2019 Skin friction measurements of systematically-varied roughness: probing the role of roughness amplitude and skewness. *Flow Turbul. Combust.* **104** (2-3), 317–329.

Flack, K. A., Schultz, M. P., Barros, J. M. & Kim, Y. C. 2016 Skin-friction behavior in the transitionally-rough regime. *Int. J. HeatFluid Flow* **61**, 21–30.

Flack, K. A., Schultz, M. P. & Volino, R. J. 2020 The effect of a systematic change in surface roughness skewness on turbulence and drag. *Int. J. Heat Fluid Flow* **85**.

Forooghi, P., Stroh, A., Magagnato, F., Jakirlić, S. & Frohnapfel, B. 2017 Toward a universal roughness correlation. *J. Fluids Eng.* **139** (12), 121201.

Jouybari, M. A., Yuan, J., Brereton, G. J. & Murillo, M. S. 2021 Data-driven prediction of the equivalent sand-grain height in rough-wall turbulent flows. *J. Fluid Mech.* **912**, A8.

Kevin, K., Kogios, A., Will, J., Tsigaras, L., Monty, J. & Hutchins, N. 2025 AQUAMARS: An Operational Support System for Quantifying the Hydrodynamic Effects from Hull Roughness. In *Proc. Int. Mar. Conf.*.

Macdonald, R. W., Griffiths, R. F. & Hall, D. J. 1998 An improved method for the estimation of surface roughness of obstacle arrays. *Atmos. Environ.* **32** (11), 1857–1864.

Medjnoun, T., Aguiar Ferreira, M., Reinartz, R., Nugroho, B., Monty, J. P., Hutchins, N. & Ganapathisubramani, B. 2023 Assessment of aerodynamic roughness parameters of turbulent boundary layers over barnacle-covered surfaces. *Exp. Fluids* **64** (11), 169.

Meneveau, C., Hutchins, N. & Chung, D. 2024 The wind-shade roughness model for turbulent wall-bounded flows. *J. Fluid Mech.* **1001**, A3.

Monty, J. P., Dogan, E., Hanson, R., Scardino, A. J., Ganapathisubramani, B. & Hutchins, N. 2016 An assessment of the ship drag penalty arising from light calcareous tubeworm fouling. *Biofouling* **32** (4), 451–464.

Nugroho, B., Monty, J. P., Utama, I. K. A. P., Ganapathisubramani, B. & Hutchins, N. 2021 Non–type behaviour of roughness when in-plane wavelength approaches the boundary layer thickness. *J. Fluid Mech.* **911**, A1.

Perry, A. E. 1982 *Hot-Wire Anemometry*. Oxford: Clarendon Press.

Ramani, A., Schilt, L., Nugroho, B., Busse, A., Jelly, T. O., Monty, J. P. & Hutchins, N. 2024 An assessment of effective slope as a parameter for turbulent drag prediction over multi-scaled roughness. *Exp. Fluids* **65** (6), 1–15.

Schlichting, H. 1937 *Experimental investigation of the problem of surface roughness*. National Advisory Commitee for Aeronautics.

Squire, T., D., Morrill-Winter, C., Hutchins, N., Schultz, M. P., Klewicki, J. C. & Marusic, I. 2016 Comparison of turbulent boundary layers over smooth and rough surfaces up to high reynolds numbers. *J. Fluid Mech.* **795**, 210–240.

Will, J.B., 'Aliman, I., Nugroho, B., Hendriyadi, Mulia, T., Taufany, F., Suastika, I. K., Utama, I. K. A. P., Schultz, M. P., Monty, J. P. & Hutchins, N. 2026 A validated tool to predict drag penalty due to hull roughness directly from hull-scan data. In *14th International Symposium on Turbulence and Shear Flow Phenomena, TSFP 2026*.

Womack, K. M., Volino, R. J., Meneveau, C. & Schultz, M. P. 2022 Turbulent boundary layer flow over regularly and irregularly arranged truncated cone surfaces. *J. Fluid Mech.* **933**, A14.